RESEARCH ARTICLE
PLANETARY SCIENCES

Earth and Planetary Physics
9: 511–520, 2025
doi: 10.26464/epp2025067

In-flight calibration of the fluxgate magnetometer on Macau Science Satellite-1

YiXin Qiu[1,2], Ying Zhang[1,2*], YaSong Ge[1,2], AiMin Du[1,2], ShuQuan Sun[1,2], Lin Zhao[1,2], Hao Luo[1,2], Lei Wang[1,2], Lin Tian[1,2], Zhi Li[1,2], and Xiao Feng[1,2]

[1]Key Laboratory of Deep Petroleum Intelligent Exploration and Development, Institute of Geology and Geophysics, Chinese Academy of Sciences, Beijing 100029, China;

[2]College of Earth Science, University of Chinese Academy of Sciences, Beijing 100049, China

Key Points:

- In-flight calibration of the fluxgate magnetometer (FGM) was performed using scalar magnetic field data from the CDSM onboard Macau Science Satellite-1.
- Euler angles were estimated through two approaches for a low-inclination satellite: using the CHAOS-7 geomagnetic field model and simultaneous estimation together with spherical harmonic coefficients.
- Calibrated FGM data are found suitable for advancing geomagnetic field scientific research.

Citation: Qiu, Y. X., Zhang, Y., Ge, Y. S., Du, A. M., Sun, S. Q., Zhao, L., Luo, H., Wang, L., Tian, L., Li, Z., and Feng, X. (2025). In-flight calibration of the fluxgate magnetometer on Macau Science Satellite-1. *Earth Planet. Phys.*, *9*(3), 511–520. http://doi.org/10.26464/epp2025067

Abstract: High-precision magnetic field measurements are crucial for understanding Earth's internal structure, space environment, and dynamic geomagnetic variations. Data from the Fluxgate Magnetometer (FGM) on the Macau Science Satellite-1A (MSS-1A), added to data from other space-based magnetometers, should increase significantly the ability of scientists to observe changes in Earth's magnetic field over time and space. Additionally, the MSS-1A's FGM is intended to help identify magnetic disturbances affecting the spacecraft itself. This report focuses on the in-flight calibration of the MSS-1 FGM. A scalar calibration, independent of geomagnetic field models, was performed to correct offsets, sensitivities, and misalignment angles of the FGM. Using seven months of data, we find that the in-flight calibration parameters show good stability. We determined Euler angles describing the rotational relationship between the FGM and the Advanced Stellar Compass (ASC) coordinate system using two approaches: calibration with the CHAOS-7 geomagnetic field model, and simultaneous estimation of Euler angles and Gaussian spherical harmonic coefficients through self-consistent modeling. The accuracy of Euler angles describing the rotation was better than 18 arcsec. The calibrated FGM data exhibit good agreement with the calibrated data of the Vector Field Magnetometer (VFM), which is the primary vector magnetometer of the satellite. These calibration efforts have significantly improved the accuracy of the FGM measurements, which are now providing reliable data for geomagnetic field studies that promise to advance our understanding of the Earth's magnetic environment.

Keywords: Macau Science Satellite-1 (MSS-1); in-flight calibration; Euler angles estimation; geomagnetic fields model; fluxgate magnetometer

1. Introduction

The Macau Science Satellite-1 (MSS-1), launched on May 21, 2023, consists of two satellites, A and B. Both satellites operate in near-circular orbits with an inclination of approximately 41° and an altitude of about 450 km. The primary objectives of MSS-1 are to monitor the South Atlantic Geomagnetic Anomaly and to obtain high-resolution lithospheric magnetic field distributions at low latitudes.

First author: Y. X. Qiu, qiuyixin22@mails.ucas.ac.cn
Correspondence to: Y. Zhang, yzhang@mail.iggcas.ac.cn
Received 31 DEC 2024; Accepted 22 MAR 2025.
First Published online 18 APR 2025.

MSS-1 satellite A is equipped with a scalar Coupled Dark State Magnetometer (CDSM), a Vector Field Magnetometer (VFM), a Fluxgate Magnetometer (FGM), and a micro Advanced Stellar Compass (ASC). The CDSM is mounted at the tip of a 4 meter-long boom, minimizing the influence of the spacecraft's magnetic interference. The VFM and ASC are closely co-located on an optical bench situated 3.6 m away from the satellite body, ensuring precise attitude determination and vector magnetic field measurements (Zhang K, 2023; Yan Q et al., 2023; Jiang Y et al., 2024). In contrast, the FGM is positioned 2 m away from the satellite body, where it is comparatively more susceptible to magnetic disturbances from the spacecraft.

The FGM instrument is a ring core system with vector-compensation consisting of a three-axis fluxgate sensor unit and a digital

signal processing electronics unit. The tri-axial ring core fluxgate sensing and the real-time vector compensating feedback technology have been developed to measure vector magnetic fields in space with low noise level at high resolution (Zhang TL et al., 2006; Auster et al., 2007, 2008; Herčík et al., 2017; Du AM et al., 2020). Compared to other magnetic sensors, such as VFM and CDSM, the FGM is relatively close to the satellite body; thus, it can also monitor and diagnose interference from the satellite platform. Like all fluxgate magnetometers, the FGM is not an absolute instrument, and hence it has to be calibrated (Lancaster et al., 1980; Olsen et al., 2000a, 2003). In addition, due to factors including aging of the material, thermal environment, launch stresses, and stress relief between the pre-flight non-vacuum and the in-flight vacuum environment, and energetic particle radiation dose effects on the magnetometer electronics (Olsen et al., 2003), it was understood that pre-flight instrument parameters would need to be observed for changes over time; thus, in-flight calibration was essential to verify the accuracy of FGM instrument response.

While vector calibration is generally superior to scalar calibration when the magnetic field vector is known (Olsen et al., 2003), in the MSS-1 mission, scalar calibration is more suitable for estimating the FGM response because the scalar magnetic field intensity is directly measured by the CDSM. However, scalar data alone cannot estimate the rotation between the FGM coordinate system and the reference system (the coordinate system of the ASC). This rotation can be determined using two different approaches: simultaneously solving for the spherical harmonic coefficients and Euler angles, and employing known magnetic field models to derive the Euler angles (Olsen et al., 2000a, 2003).

The content of this paper is organized as follows. In Section 2, we analyze the response characteristics of the FGM as a linear magnetometer and estimate its response parameters through an in-flight scalar calibration. In Section 3, we focus on the estimation of the Euler angles that describe the rotational relationship between the FGM and ASC coordinate systems. Two different methods are applied to estimate Euler angles for a low-inclination satellite. In the first method, the CHAOS-7 geomagnetic field model is utilized as a reference; the second employs a self-consistent geomagnetic field model derived from MSS-1 and Swarm satellite observations. Discussion and conclusions are given in Section 4.

2. In-flight Scalar Calibration of the FGM Instrument

As previously stated, the parameters of the vector magnetometer will change over time due to effects of the in-flight vacuum environment and exposure to energetic particle radiation. Consequently, the intrinsic parameters of the FGM instrument need to be recalibrated throughout the mission. Two methods are available for calibrating a magnetometer: vector calibration, which compares the instrument's readings to a known magnetic field vector, and scalar calibration, which relies solely on the magnetic field intensity. When the actual magnetic field vector is known, vector calibration is generally more effective than scalar calibration. However, the vector field is often estimated using a geomagnetic field model; scalar calibration is thus more advantageous for determining intrinsic parameters in cases such as this one, in which the MSS-1's CDSM scalar magnetometer offers stable absolute measurements of magnetic field intensity and is positioned at the ends of a 4-meter boom, minimizing magnetic interference from the spacecraft. Therefore, we judged that the CDSM measurements can be reliably used for in-flight scalar calibration of the FGM.

Previous studies have proved that fluxgate magnetometer is a kind of linear instrument (Risbo and Olsen, 1996; Merayo et al., 2000; Risbo et al., 2001; Olsen et al., 2003). Under an ideal sensor orthogonal coordinate system, the relationship between the real magnetic field intensity $\boldsymbol{B}_{\rm FGM}$ and the sensor output $\boldsymbol{F}$ is

$$\boldsymbol{F} = \boldsymbol{S}\cdot\boldsymbol{P}\cdot\boldsymbol{B}_{\rm FGM} + \boldsymbol{b},$$

where

$$\boldsymbol{b} = \begin{pmatrix} b_1 \\ b_2 \\ b_3 \end{pmatrix}$$

is the vector of offset,

$$\boldsymbol{S} = \begin{pmatrix} S_1 & 0 & 0 \\ 0 & S_2 & 0 \\ 0 & 0 & S_3 \end{pmatrix}$$

is the matrix of sensitivities, and

$$\boldsymbol{P} = \begin{pmatrix} 1 & 0 & 0 \\ -\sin u_1 & \cos u_1 & 0 \\ \sin u_2 & \sin u_3 & \sqrt{1-\sin^2 u_2 - \sin^2 u_3} \end{pmatrix}$$

is a matrix that transforms a vector from the orthogonal magnetometer coordinate system to the non-orthogonal magnetometer coordinate system. These 9 intrinsic parameters $b_i, S_i, u_i, i = 1, 2, 3$ describe the response of a linear magnetometer; this parameterization method was proposed by Risbo and Olsen in 1996 (Risbo and Olsen, 1996). Laboratory measurements and pre-inflight calibrations have shown that the sensitivities S_i and the offsets b_i also depend linearly on the sensor temperature and the electronics temperature (Nielsen et al., 1995; Olsen et al., 2003). Ground calibration parameters before launch have been used to correct FGM outputs for temperature dependence.

Once the calibration parameters are determined, the magnetic field in the FGM coordinate system can be derived:

$$\begin{aligned} \boldsymbol{B}_{\rm FGM} &= |\boldsymbol{B}_{\rm FGM}| = \sqrt{\boldsymbol{B}_{\rm FGM}^{\rm T}\cdot\boldsymbol{B}_{\rm FGM}} \\ &= \sqrt{(\boldsymbol{F}-\boldsymbol{b})^{\rm T}\cdot\boldsymbol{S}^{-1}(\boldsymbol{P}^{-1})^{\rm T}\boldsymbol{P}^{-1}\boldsymbol{S}^{-1}(\boldsymbol{F}-\boldsymbol{b})}, \end{aligned} \tag{1}$$

where $\boldsymbol{P}^{-1}$ is

$$\boldsymbol{P}^{-1} = \begin{pmatrix} 1 & 0 & 0 \\ \dfrac{\sin u_1}{\cos u_1} & \dfrac{1}{\cos u_1} & 0 \\ -\dfrac{\sin u_1 \sin u_3 + \cos u_1 \sin u_2}{\omega \cos u_1} & -\dfrac{\sin u_3}{\omega \cos u_1} & -\dfrac{1}{\omega} \end{pmatrix} \tag{2}$$

with $\omega = \sqrt{(1-\sin^2 u_2 - \sin^2 u_3)}$.

Using a nonlinear least-squares approach to estimate these 9 parameters, the objective function is

$$\chi^2 = \sum\left(\frac{\boldsymbol{B}_{\rm FGM}(\boldsymbol{F},\boldsymbol{m}) - \boldsymbol{B}_{\rm CDSM}}{\sigma_B}\right)^2 = \text{Min!}, \tag{3}$$

where the $\boldsymbol{B}_{\mathrm{FGM}}(\boldsymbol{F},\boldsymbol{m})$ is determined by the sensor output F and the model parameter vector $\boldsymbol{m}=(b_i,S_i,u_i)^{\mathrm{T}}$. The $\boldsymbol{B}_{\mathrm{CDSM}}$ is the scalar magnetic field measured by CDSM, which is considered to be the correct filed intensity. σ_B is the data error, and for simplicity, all data points are assumed to have the same error, so σ_B is a constant.

The data residuals $\delta\boldsymbol{d}=\boldsymbol{B}_{\mathrm{FGM}}(\boldsymbol{F},\boldsymbol{m})-\boldsymbol{B}_{\mathrm{CDSM}}$ can be approximated linearly by the model vector $\boldsymbol{m}=(b_i,S_i,u_i)^{\mathrm{T}}$ as follows:

$$\delta\boldsymbol{d}_i=\underline{\underline{\boldsymbol{G}}}_i\cdot\delta\boldsymbol{m}_i, \tag{4}$$

where the superscript i represents the ith iteration; therefore the core matrix $\underline{\underline{\boldsymbol{G}}}_i$ can be defined as follows:

$$\underline{\underline{\boldsymbol{G}}}_i=\frac{\partial d(\boldsymbol{m})}{\partial\boldsymbol{m}}\Big|_{\boldsymbol{m}=\boldsymbol{m}_i}, \tag{5}$$

The ith iteration of least-squares can be written as

$$\boldsymbol{m}_{i+1}=\boldsymbol{m}_i+\delta\boldsymbol{m}_i, \tag{6}$$

$$\delta\boldsymbol{m}_i=\left[(\underline{\underline{\boldsymbol{G}}}_i)^{\mathrm{T}}\cdot\underline{\underline{\boldsymbol{W}}}\cdot\underline{\underline{\boldsymbol{G}}}_i\right]^{-1}\left[(\underline{\underline{\boldsymbol{G}}}_i)^{\mathrm{T}}\cdot\underline{\underline{\boldsymbol{W}}}\cdot(d-d(\boldsymbol{m}_i))\right], \tag{7}$$

where the $\underline{\underline{\boldsymbol{W}}}$ is the Huber weight matrix, which is used to adjust the contribution rate of different observations to the loss function (Hogg, 1979).

The in-flight scalar calibration should be implemented as follows:

- Calibrate the FGM measurements using the ground calibration parameters;
- Obtain the non-linear least-squares solution for FGM measurements using Equation (3), iteratively deriving the calibration coefficients ($\boldsymbol{S}$, $\boldsymbol{P}$, and $\boldsymbol{b}$);
- Apply the nine intrinsic parameters of the FGM sensor: three sensitivities, three misalignment angles, and three offsets to the sensor output ($\boldsymbol{F}$) according to Equation (1).

To minimize instrument drift over time, we conducted a scalar calibration of these nine intrinsic parameters of the FGM daily throughout the mission. To study the long-term stability of the instrument, the calibration was performed separately for each day between November 1, 2023 and May 28, 2024. Figure 1 shows the sensitivities, misalignment angles, the offset, electronics temperature, and sensor temperature for each of the 201 days and for the three axes. By averaging over all 201 days, mean values for the calibration parameters were obtained (Table 1). Standard deviations from the linear trend were derived from the scatter of the 201 values shown in Figure 1. The offsets reaching −39.53 nT are likely caused by static interference from the spacecraft that was not considered during pre-flight calibration. Taking into account that the pre-flight tests were conducted without the full flight configuration (for instance, the solar panels were not operational), we estimated the parameters of the instruments in conjunction with static magnetic interference, allowing us to estimate how the permanent magnetic field produced by the spacecraft would contribute to the offsets. The magnetic interference along axis 1, which runs along the boom and is considered positive towards the spacecraft, is greater than that along the other two axes. Calibration parameter plots indicate that the FGM vector magnetometer is stable, with deviations from the linear trend remaining under 3 nT for offsets, under 150 ppm for sensitivities, and under 0.007° for misalignment angles. Note that a noticeable drift in the sensitivities occurred over time, particularly for axes 2 and 3, which was influenced by sensor temperature. The time-related changes in sensitivities are likely linked to the aging of the magnetometer's electronics due to the effects of particle radiation.

3. Estimation of the Euler Angles Between FGM and ASC Coordinate Systems

Euler angles α,β,γ, are used to describe the rotation relationship between the FGM sensor coordinate system and the ASC coordinate system. These three angles can be determined by comparing the magnetic vector in the FGM coordinate system (whose orientation is unknown) with that in the ASC coordinate system. The magnetic vector in the ASC coordinate system is obtained from rotating the Earth's magnetic field vector, which can be calculated using existing magnetic field models or can be modeled by a scalar potential. That is to say that there are two ways to solve the Euler angles.

The rotation matrix $\underline{\underline{\boldsymbol{T}}}$ which transfers the magnetic vector from a local north, east, center (NEC) spherical coordinate system to the coordinate system of ASC is measured by the star sensor. The final rotation relationship of the FGM magnetic vector can be expressed as:

$$\boldsymbol{B}_{\mathrm{FGM}}=\underline{\underline{\boldsymbol{R}}}(\boldsymbol{\varepsilon})\cdot\boldsymbol{B}_{\mathrm{ASC}}=\underline{\underline{\boldsymbol{R}}}(\boldsymbol{\varepsilon})\cdot\underline{\underline{\boldsymbol{T}}}\cdot\boldsymbol{B}_{\mathrm{NEC}}=-\underline{\underline{\boldsymbol{R}}}(\boldsymbol{\varepsilon})\cdot\underline{\underline{\boldsymbol{T}}}\cdot\mathrm{grad}\,V, \tag{8}$$

where $\boldsymbol{\varepsilon}=(\alpha,\beta,\gamma)^{\mathrm{T}}$, and $\underline{\underline{\boldsymbol{R}}}(\boldsymbol{\varepsilon})$ is the transformation method of a "3-2-3" rotation. $\boldsymbol{B}_{\mathrm{NEC}}=(N,E,C)^{\mathrm{T}}=(-B_\vartheta,B_\phi,-B_r)^{\mathrm{T}}$, and the magnetic scalar potential V is expanded into a series of spherical harmonics.

3.1 Using the CHAOS-7 Model for Euler Angles Determination

For this approach we utilized $\boldsymbol{B}_{\mathrm{NEC}}$ from the CHAOS-7 model, which is a high-precision geomagnetic field model developed using data from multiple satellites, such as Swarm and CryoSat-2, as well as ground-based observatories. Covering the period from 1999 to 2020, this model provides accurate and time-resolved geomagnetic field values, making it an excellent reference for calibrating magnetometers on spacecraft (Finlay et al., 2020).

By comparing the satellite's magnetometer measurements with the geomagnetic field values predicted by the CHAOS-7 model, discrepancies can be minimized through adjustments to the Euler angles. This process ensures alignment between the satellite's measured magnetic field vectors and the model's reference values, enhancing the accuracy of the instrument's readings in the Earth's coordinate system.

In order to reduce the error from the unmodeled signals in the CHAOS-7 model as much as possible, we selected geomagnetic field data during magnetically quiet periods ($|Dst|<15$ nT, $Kp<2$) to minimize external field disturbances and enhance calibration accuracy. The results, as shown in Figure 3, yield *mean* Euler angles of $\alpha=89.93°\pm0.019°$, $\beta=55.33°\pm0.009°$, $\gamma=0.41°\pm0.014°$. Notably, the Euler angles exhibit periodic variations with a cycle of approximately two months. As illustrated in Figure 2, the MMS-1 satellite exhibits a drift in magnetic local time at an approximate

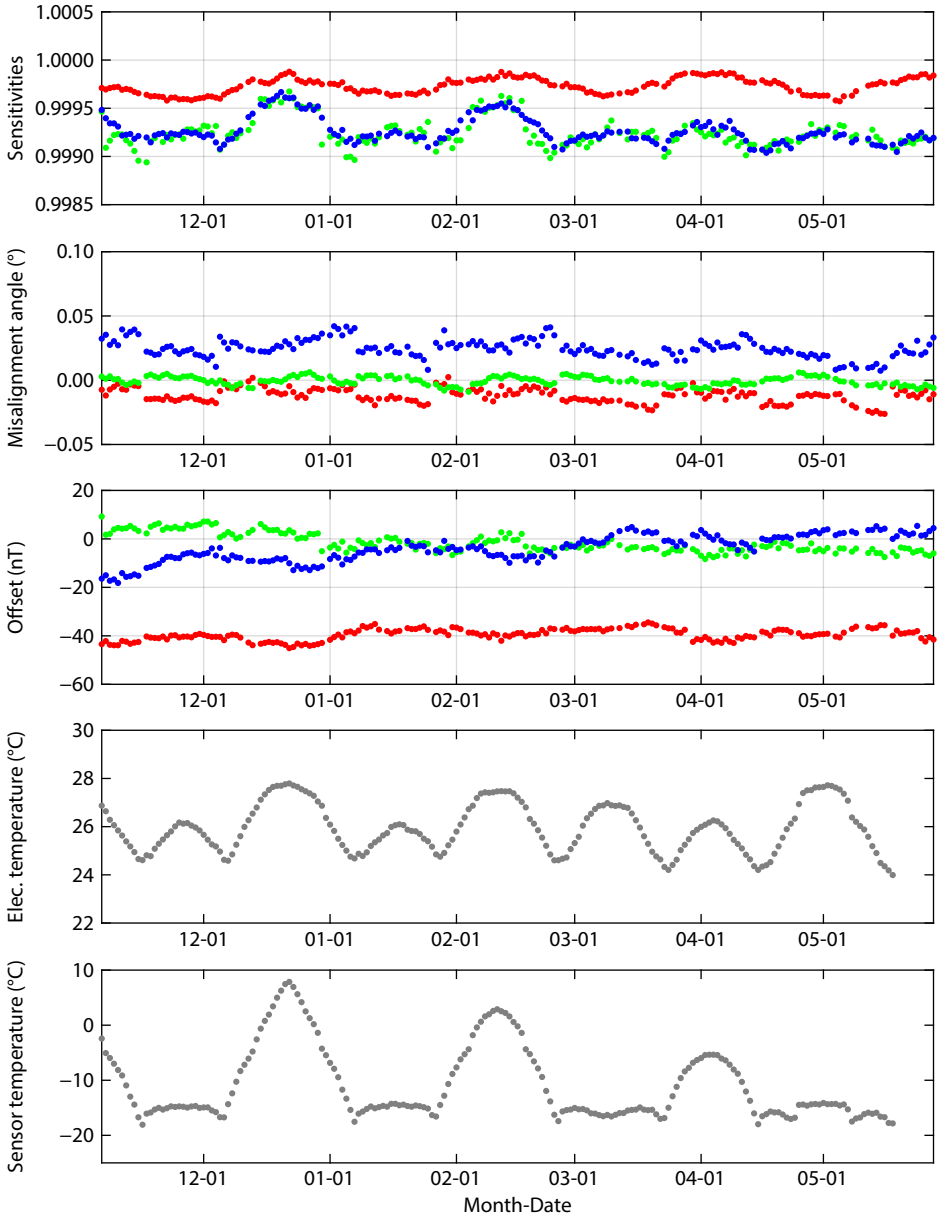

Figure 1. Scatter of the sensitivities, misalignment angles, the offset, electronics temperature and sensor temperature for 201 days between November 1, 2023 and May 28, 2024 and for the three axes (axis 1: red; axis 2: blue; axis 3: green).

Table 1. Results of the in-flight scalar calibration.

	Axis 1	Axis 2	Axis 3
Offsets (nT)	−39.53 ± 2.18	−1.54 ± 2.34	−4.08 ± 2.76
Sensitivities	$0.9997 \pm 7.8 \times 10^{-5}$	$0.9992 \pm 1.5 \times 10^{-4}$	$0.9993 \pm 1.4 \times 10^{-4}$
Misalignment angles (°)	−0.0118 ± 0.005	−0.0005 ± 0.003	0.0248 ± 0.007

rate of 13.8 hours per month; thus the satellite revisits the same magnetic local time approximately every 52 days. A notable correlation exists between the two-month periodicity observed in the variations of the Euler angles and the orbital precession cycle of the satellite. However, no analogous periodic pattern was detected in the drift of the instrument parameters over time. Therefore, the most probable cause of periodic variations of Euler angles is related to the estimation errors from unmodeled external field signals also exhibiting about two-month periodicity with the precession of the satellite's orbit.

One month of data (November 20 to December 20, 2023) was selected to analyze the residuals between the CHAOS-7 model values and MSS-1 FGM measurements (Figure 3) as well as between VFM and FGM measurements (Figure 4), providing a statistical basis for evaluating the in-flight performance of FGM

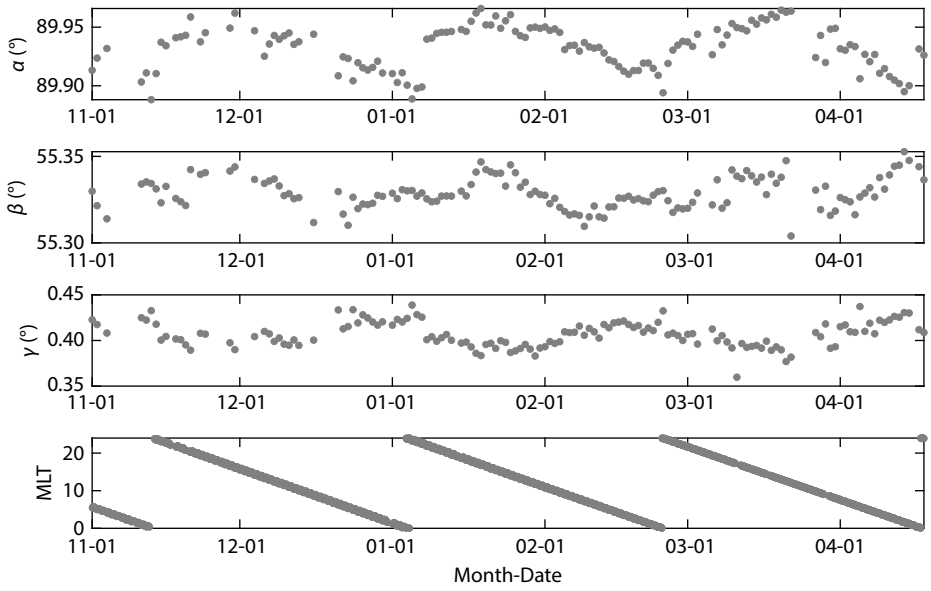

Figure 2. The Euler angles α, β and γ describing the FGM-ASC rotation as found from independent data segments between November 2023 and April 2024. (Bottom) Magnetic local time at the equator (northward tracks) over the same time interval.

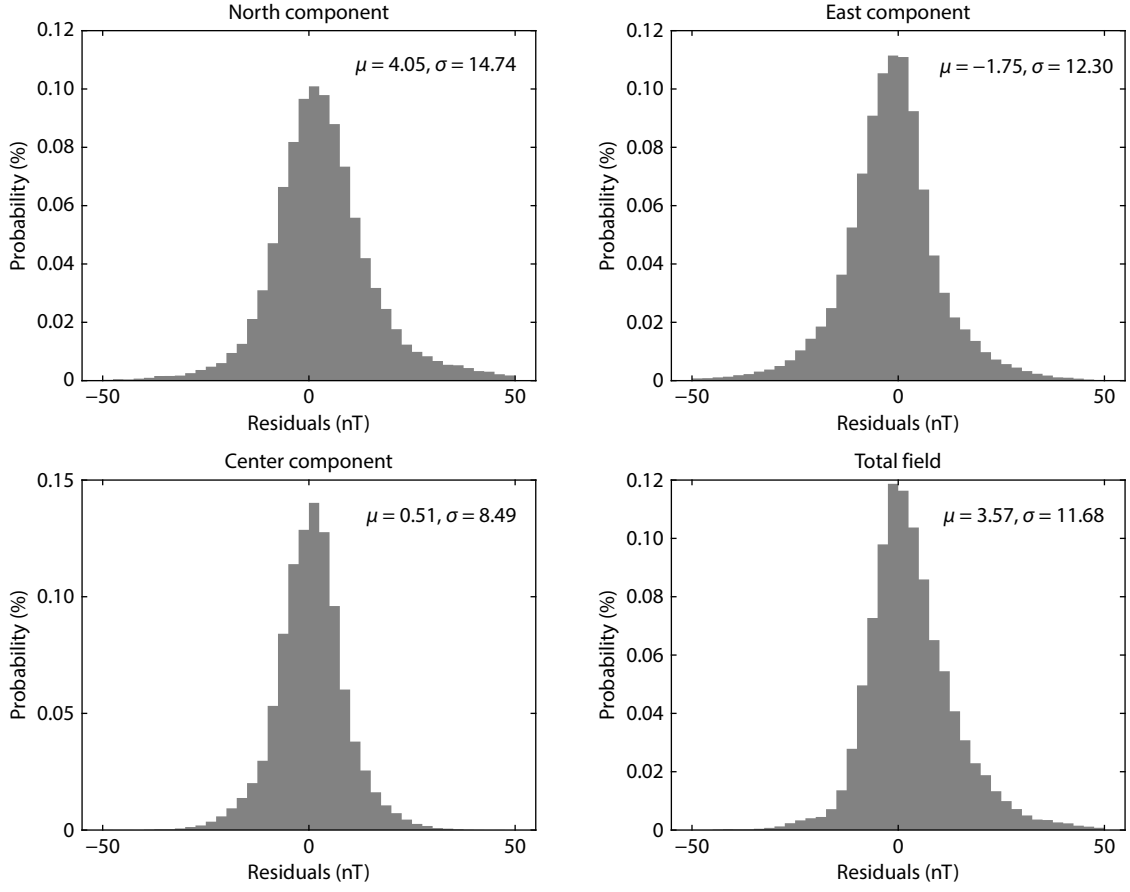

Figure 3. Histograms showing distribution of residuals between CHAOS-7 predictions and FGM data from Nov 20, 2023 to Dec 20, 2023.

instruments.

Figure 3 shows the residuals between the magnetic field data from the FGM and the CHAOS-7 geomagnetic field model after transforming the FGM data into the NEC coordinate system using the calibrated Euler angles. The four subplots display the residual distributions for the North, East, Center (vertical), and total field components, with mean values (μ) of 4.05, −1.75, 0.51, and 3.57 nT, and standard deviations (σ) of 14.74, 12.30, 8.49, and 11.68 nT, respectively. The residuals are centered around zero with relatively small spreads, confirming that the calibrated Euler

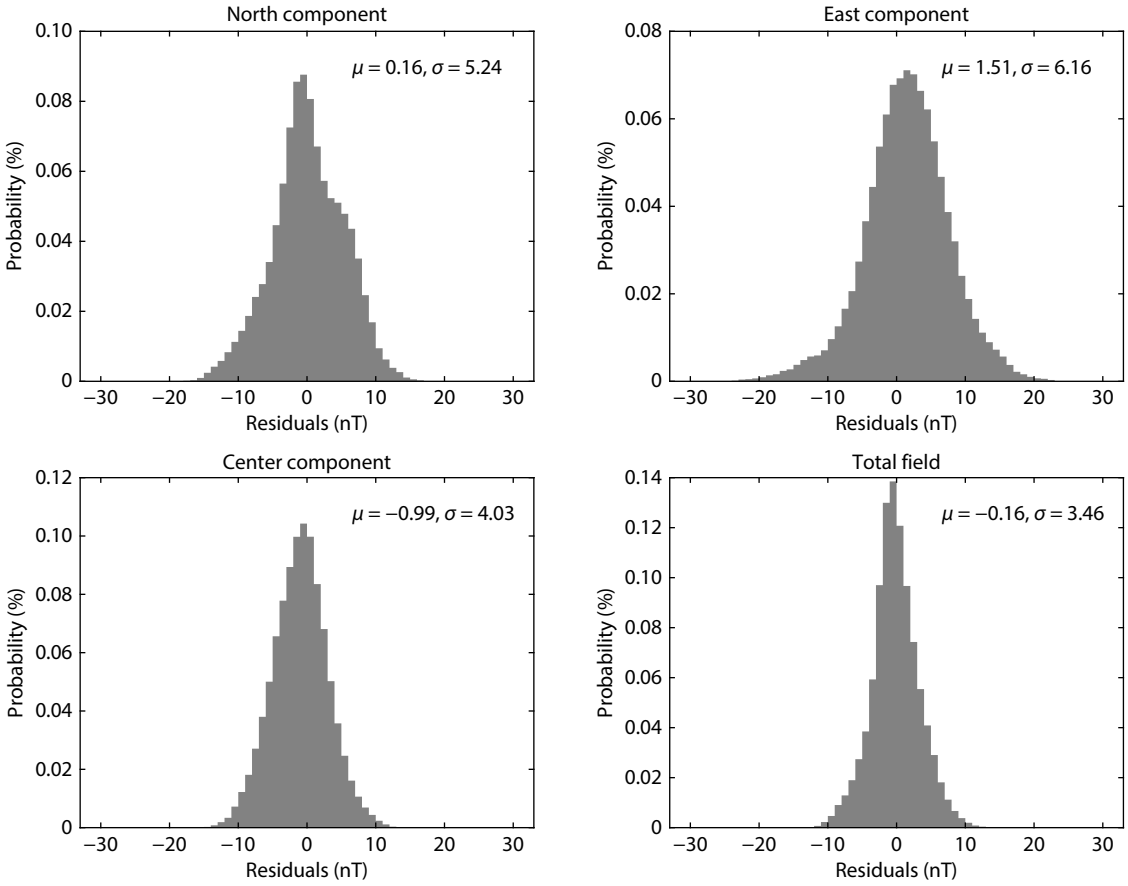

Figure 4. Histograms showing distribution of residuals between VFM data and FGM data from Nov 20, 2023 to Dec 20, 2023.

angles effectively aligned the FGM data with the CHAOS-7 model and demonstrating the accuracy of the calibration process. It should also be noted that the residuals may contain the magnetic field generated by the magnetic field continuation error from the difference between the altitudes of MSS-1 and Swarm and the unmodeled external field signals in the CHAOS-7 model, such as the solar quiet (*Sq*) current, equatorial electrojet (EEJ), and large-scale F region currents.

Figure 4 shows the residual distributions between the magnetic field measurements from the VFM and the FGM. The mean values (μ) of the residuals for the North, East, Center (vertical), and total field components are 0.16, 1.51, −0.99, and −0.16 nT, with standard deviations (σ) of 5.24, 6.16, 4.03, and 3.46 nT, respectively. While most components display symmetric and approximately normal distributions, the North component shows a slight deviation, likely due to micro-deformation of the boom affecting the relative attitudes of FGM to ASC. Overall, the results indicate good agreement between the VFM and FGM data.

3.2 Simultaneous Estimation of Euler Angles Together with Geomagnetic Spherical Harmonic Model

We present a geomagnetic field model refined from the framework established by Olsen (Olsen, 2002), in which the secular variation of the main magnetic field has been removed. This adjustment is made because the observation period of the FGM is relatively short, making it challenging to detect secular variation. Additionally, the ring current (*RC*) index used in Olsen's model has been replaced with the *Dst* index, as the *Dst* index is more readily available. The refined model is employed to solve simultaneously the spherical harmonic coefficients of the geomagnetic field and to calibrate the Euler angles.

$$V = a\left\{\sum_{n=1}^{N_{\mathrm{IN}}}\sum_{m=0}^{n}\left(g_n^m\cos m\phi + h_n^m\sin m\phi\right)\left(\frac{a}{r}\right)^{n+1}P_n^m(\cos\vartheta)\right.$$
$$+\sum_{n=1}^{N_{\mathrm{EX}}}\sum_{m=0}^{n}\left(q_n^m\cos m\phi + s_n^m\sin m\phi\right)\left(\frac{r}{a}\right)^{n}P_n^m(\cos\vartheta)$$
$$\left.+\,Dst\cdot\left[\left(\frac{r}{a}\right)+Q_1\left(\frac{a}{r}\right)^2\right]\times\left[\sum_{m=0}^{1}\left(\tilde{q}_1^m\cos m\phi+\tilde{s}_1^m\sin m\phi\right)P_1^m(\cos\vartheta)\right]\right\}, \tag{9}$$

a = 6371.2 km is the mean radius of the Earth, (r, ϑ, ϕ) are geographical coordinates. P_n^m are the associated Schmidt-normalized Legendre function of degree n and order m. (g_n^m, h_n^m) and (q_n^m, s_n^m) are the Gauss coefficients describing sources internal and external to the Earth. The last coefficients $(\tilde{q}_1^m, \tilde{s}_1^m)$ describe the contribution of the varying magnetospheric ring current magnetic field to the model, which is considered by means of the factor Q_1 = 0.27 (Langel and Estes, 1985). The *Dst* index is also used for data selection. The maximum degree of the spherical harmonic expansion is chosen to N_{IN} = 19 for the internal field and up to N_{EX} = 3 for the external field.

As a low orbital inclination satellite, the MSS-1 can measure the magnetic field in the Earth's latitude only below 41°. So we used Swarm's polar magnetic field data to make up for Earth latitudes

above 41°. To minimize the influence of external field-aligned current systems at polar latitudes, we used scalar magnetic field intensity in regions with magnetic latitudes greater than 55°.

The data vector

$$\boldsymbol{d} = \left(\boldsymbol{B}_{\mathrm{FGM}}^{\mathrm{T}}, \boldsymbol{B}_{\mathrm{Swarm}}^{\mathrm{T}}, \overline{\boldsymbol{B}}_{\mathrm{Swarm}}^{\mathrm{T}}\right)^{\mathrm{T}}$$

consists of a first part

$$\boldsymbol{B}_{\mathrm{FGM}} = \left(X_1, Y_1, Z_1, \ldots, X_{N_{\mathrm{FGM}}}, Y_{N_{\mathrm{FGM}}}, Z_{N_{\mathrm{FGM}}}\right)^{\mathrm{T}}$$

containing the N_{FGM} calibrated vector field measurements from the vector magnetometer in its orthogonal FGM system, and a second part

$$\boldsymbol{B}_{\mathrm{Swarm}} = \left(\dot{X}_1, \dot{Y}_1, \dot{Z}_1, \ldots, \dot{X}_{N_{\mathrm{Swarm}}}, \dot{Y}_{N_{\mathrm{Swarm}}}, \dot{Z}_{N_{\mathrm{Swarm}}}\right)^{\mathrm{T}}$$

contain the N_{Swarm} vector field measurements from the Swarm satellite. The third part $\overline{\boldsymbol{B}}_{\mathrm{Swarm}}^{\mathrm{T}}$ is the scalar data of Swarm satellite. Similarly, the model vector

$$\boldsymbol{m} = \left(\boldsymbol{g}^{\mathrm{T}}, \boldsymbol{\varepsilon}^{\mathrm{T}}\right)^{\mathrm{T}}$$

consists of a first part

$$\boldsymbol{g} = (\ldots, g_n^m, h_n^m, q_n^m, s_n^m, \tilde{q}_1^m, \tilde{s}_1^m \ldots)^{\mathrm{T}},$$

which contains the Gauss coefficients of the spherical harmonic expansion, and a second part $\boldsymbol{\varepsilon} = (\alpha, \beta, \gamma)^{\mathrm{T}}$ containing the three Euler angles describing the "3-2-3" rotation $\underline{\boldsymbol{R}}(\boldsymbol{\varepsilon})$.The Euler angles and the Gauss coefficients of the field model were estimated by an iterative Gauss least-squares estimator just as in Section 2.

In order to select data during a quiet period of the Earth's magnetic field, to reduce the influence of the Earth's ring current or the polar caps, we also screened the data as follows:

- $Kp \leq 2$ for the time;
- Night-side data of magneticlocaltime (MLT) ≥ 21 and MLT ≤ 3;
- The index of magnetospheric ring-current strength, *Dst*, within 10 nT and $|\mathrm{d}(Dst)/\mathrm{d}(t)| < 3$ nT/h;
- Interplanetary magnetic field $|B_y| < 3$ nT.

To avoid overfitting the model due to overly dense sampling, the data were decimated such that measurement instances were at least 30 seconds apart.

Four different models have been derived. They all have the same parameterization but differ in the data used to derive the model:

- Model MSS1-FGM (24a) is based on data from all geomagnetic quiet periods observed between November 1, 2023 and February 1, 2024.
- Model MSS1-FGM (24b) is based on data from all geomagnetic quiet periods between March 1, 2024 and April 18, 2024.
- Model MSS1-FGM (24c) is based on the MSS1-FGM (24a) model,

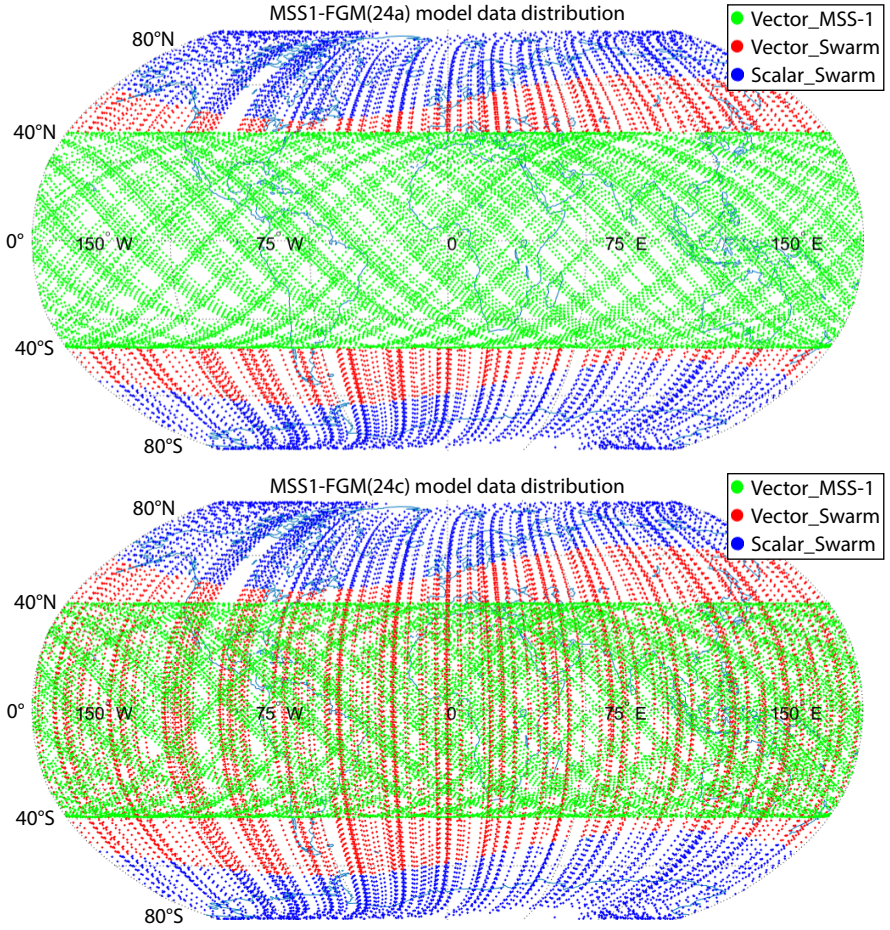

Figure 5. Data used in the MSS1-FGM (24a, 24c) model. The green symbols show the location of FGM vector data from MSS-1, the red symbols and the blue symbols are the locations of vector data and scalar data from Swarm satellites.

with the addition of vector data from Swarm satellites for latitudes less than 41°.

● Model MSS1-FGM(24d) is based on the MSS1-FGM(24b) model, again with the addition of vector data from Swarm for latitudes less than 41°.

As an example, Figure 5 shows the data distribution used for the MSS1-FGM(24a) and 24c models. A total of 27,105 magnetic field observations were used for the 24a model, including 18,123 FGM vector data from the MSS-1, and 3192 vector data and 5790 scalar data from Swarm. The 24c model, based on the 24a model, incorporates 18,123 FGM vector data, 12,488 vector data and 5790 scalar data from Swarm.

Figure 6 shows the residual histograms of the B_r component between predictions of four models, MSS1-FGM(24a, 24b, 24c, 24d), and actual FGM observations. Models MSS1-FGM(24a) and 24b use the same satellite data distribution (MSS-1 below 41° latitude, Swarm above 41°) but cover different time periods. Model MSS1-FGM(24c) introduces Swarm vector data below 41° latitude based on the 24a model. Similarly, model MSS1-FGM(24d) is based on 24b and Swarn data in the same way. The results indicate that the residuals of all four models approximate a Gaussian distribution, with slight differences in mean and standard deviation. Table 3 provides our statistical analysis of the misfit between the MSS1-FGM models (24a, 24b, 24c and 24d) and data from MSS-1 and Swarm satellites. The number of data points (N), mean misfit, and root mean square (RMS) residuals for both scalar ($F_{\rm polar}$) and vector components (B_r, B_θ, B_ϕ) are given. The Swarm scalar data in high-latitude regions ($F_{\rm polar}$) exhibit larger RMS values compared to the vector components, with model 24b showing the highest misfit. The MSS-1 vector components demonstrate relatively small mean values and RMS residuals, indicating good agreement with the models. Across all components, the residuals remain within an acceptable range, reflecting the consistency and reliability of the models in describing the observed magnetic field data.

The Euler angles of the FGM→ASC transformation are presented in Table 2. Our analysis shows a high level of consistency among the four models, with variations in α, β, and γ limited to 0.004°, 0.003° and 0.004°, respectively. This indicates that the derived Euler angles are stable and reliable across different model configurations, reflecting the robustness of the calibration process. These values differ from the mean values of the first approach by less than 18 arcsec.

To assess the accuracy of the model specified by a finite set of

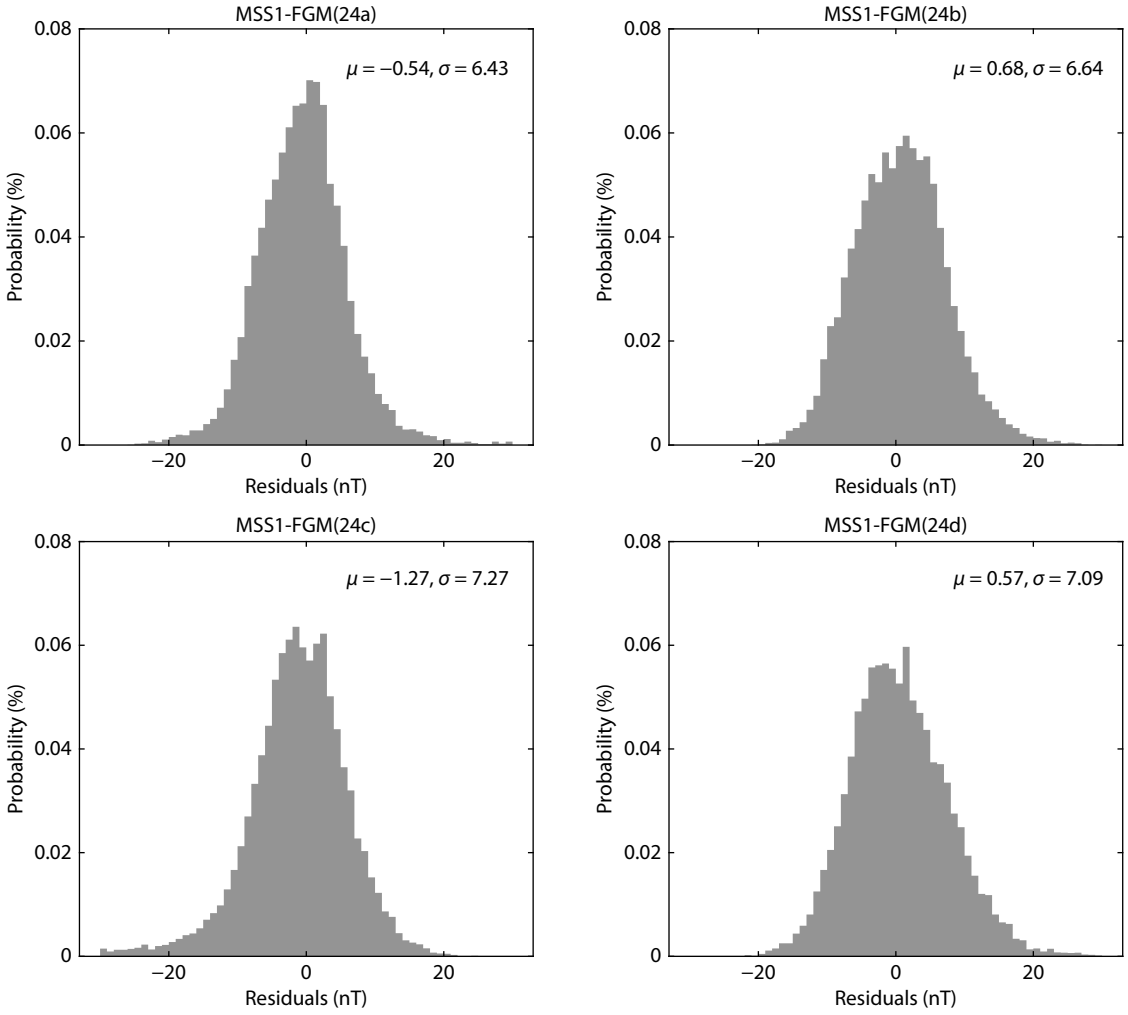

Figure 6. Histograms showing distributions of residuals between the various MSS1-FGM model predictions and actual FGM observational data.

Table 2. Euler angles derived from MSS1-FGM Models (24a, 24b, 24c, and 24d).

	α	β	γ
MSS1-FGM(24a)	89.929°	55.320°	0.417°
MSS1-FGM (24b)	89.931°	55.318°	0.413°
MSS1-FGM (24c)	89.927°	55.320°	0.415°
MSS1-FGM (24d)	89.928°	55.317°	0.416°

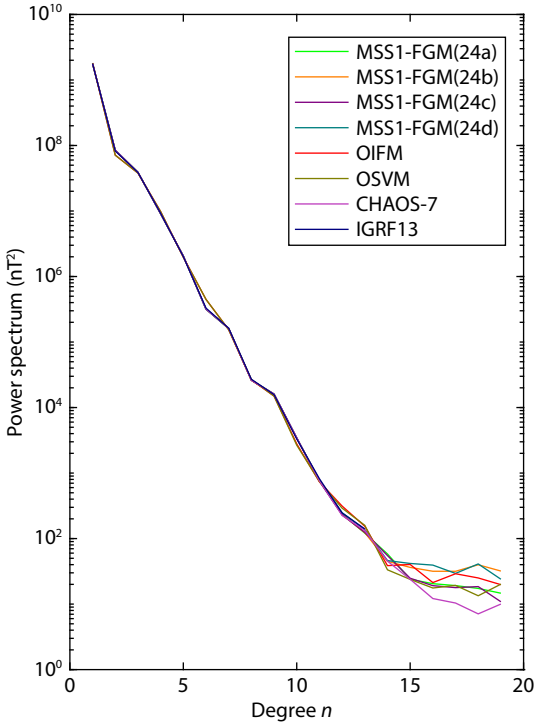

Figure 7. Comparison of the geomagnetic power spectra between the MSS1-FGM models (24a, 24b, 24c, and 24d) and the geomagnetic field models IGRF13, OIFM, OSVM, and CHAOS-7.

spherical harmonic coefficients, the Lowes–Mauersberger spherical harmonic power spectra of four MSS1-FGM models (24a, 24b, 24c and 24d) were compared with the IGRF13, OIFM (Olsen et al., 2000b), OSVM (Olsen, 2002), and CHAOS-7 geomagnetic field models (Figure 7). By investigating the distribution of magnitudes across various spatial scales, this comparison tests the consistency of our model with these other models. The power decreases with increasing spherical harmonic degree n, consistent with the expected trend for Earth's internal geomagnetic field. At lower degrees ($n \leq 14$), the MSS1-FGM models agree well with the given geomagnetic models, indicating their excellent performance in representing the main field from the Earth's core. However, at higher degrees ($n > 14$), the power spectra of the MSS1-FGM models are slightly larger than that of CHAOS-7. In addition, models 24b and 24d exhibit higher power levels than models 24a and 24c, probably due to the fact that the data of models 24b and 24d include periods of data collection that included more disturbed days. It is also possible that contributions from ionospheric current systems are present in the data and thus the models, although we attempted to reduce external current contributions by data selection according to geomagnetic indices and Interplanetary magnetic field B_y. Overall, the results demonstrate good consistency between the MSS1-FGM models and the given field models.

4. Discussion and Conclusions

In this study, we utilized data from the scalar magnetometer (CDSM) onboard MSS-1 to calibrate the 9 intrinsic parameters of the FGM instrument, including the offsets, sensitivities, and misalignment angles for the three components. Based on seven months of data, the in-flight calibration parameters exhibited good stability, with the offsets ranging from −39.53 nT ± 2.18 nT to −4.08 nT ± 2.76 nT, sensitivities from $0.9992 \pm 1.5 \times 10^{-4}$ to $0.9997 \pm 7.8 \times 10^{-5}$, and misalignment angles from $-0.0005° \pm 0.003°$ to $0.0248° \pm 0.007°$. The FGM data, corrected using these intrinsic parameters, were then used for subsequent Euler angles calibration.

The transformation between the FGM magnetometer coordinate system and the reference system of ASC was estimated by comparing the magnetic and attitude measurements with magnetic field values from an existing magnetic fields model or an independently derived model of the Earth's magnetic field. Using CHAOS-7 as a reference during geomagnetically quiet periods, precise Euler angles were derived for calibration. Over a one-month dataset, the residuals between the calibrated FGM data

Table 3. Statistics of the misfit between model and MSS-1 and Swarm satellite data.[a]

Satellite	Component	MSS1-FGM(24a)			MSS1-FGM(24b)			MSS1-FGM(24c)			MSS1-FGM(24d)		
		N	Mean	RMS	*N*	Mean	RMS	*N*	Mean	RMS	*N*	Mean	RMS
Swarm Alpha	F_{polar}	5790	9.07	47.82	6283	17.98	64.64	5790	8.91	48.07	6283	16.78	64.62
	B_r	3192	−1.32	5.98	1790	1.14	3.72	12,488	−0.26	6.13	6457	1.43	5.03
	B_θ	3192	0.63	6.44	1790	1.05	6.52	12,488	0.56	4.83	6457	0.54	4.45
	B_ϕ	3192	−0.08	6.28	1790	0.38	5.91	12,488	0.49	5.12	6457	−1.07	3.28
MSS-1	B_r	18,123	−0.53	6.44	17,103	0.68	6.64	18,123	−1.27	7.27	17,103	−1.06	7.48
	B_θ	18,123	0.94	9.44	17,103	1.90	9.13	18,123	1.13	9.53	17,103	3.04	9.25
	B_ϕ	18,123	−0.67	5.79	17,103	−0.88	7.17	18,123	−0.84	6.10	17,103	0.56	7.09

[a]Numbers of data points (*N*), Means and RMS misfits (in nT) for the different components.

and CHAOS-7 model values demonstrated excellent accuracy, with mean values below 5 nT and standard deviations under 15 nT . Similarly, the comparison between FGM and VFM measurements indicated a high degree of consistency. The residuals across components showed small mean values (ranging from −0.16 nT to 1.51 nT) and low standard deviations (ranging from 3.46 nT to 6.16 nT, suggesting good agreement between the two instruments, in spite of micro deformation of the boom affecting the relative attitudes of FGM to ASC.

In addition, for a low-inclination satellite, using FGM data from MSS-1 and Swarm satellite observations, the Euler angles were simultaneously estimated together with the spherical harmonic coefficients of the geomagnetic field. The model results demonstrated a high degree of consistency between the modeled and measured magnetic fields at low degrees. However, coefficients above degree 14 may not be robust due to the inclusion of the external field from the ionospheric current systems. The residuals between the models and MSS-1 FGM data exhibit mean values close to zero and standard deviations below 10 nT across all vector components, confirming the reliability of the models. We estimate that the Euler angles describing the transformation have an accuracy of better than 18 arcsec. These calibration results confirm that the FGM vector data had good quality and would provide reliable data for geomagnetic field studies. In comparison to the Swarm mission, the low-inclination MSS-1 satellite provides better local time coverage for vector magnetic field measurements. This improvement facilitates a more effective distinction between the temporal and spatial variations in the magnetic field, making possible the development of more precise models for the magnetospheric and ionospheric fields, as well as a model for the temporal variations of the core dynamo field. By combining MSS-1 data with global geomagnetic satellite datasets, we can expect to create a model of the Earth's geomagnetic field with higher spatial and temporal resolution. This will give us access to more comprehensive information regarding the geomagnetic core dynamo, three-dimensional mantle conductivity profiles, and characteristics of the electric current systems in the magnetosphere and ionosphere, particularly concerning the ring current, the *Sq*, and the EEJ.

Acknowledgments

This work was supported by the Macao Foundation. We acknowledge use of Swarm Data obtained from the website ftp://swarm-diss.eo.esa.int/. We are grateful to NASA/GSFC's Space Physics Data Facility's OMNIWeb and OMNIdata. The *Dst* index used in this paper was provided by the WDC for Geomagnetism, Kyoto (https://wdc.kugi.kyoto-u.ac.jp/dst_provisional/index.html). The *Kp* index data were obtained online from https://kp.gfz-potsdam.de. The MSS-1 data are available at https://mss.must.edu.mo/data.html.

References

Auster, H. U., Apathy, I., Berghofer, G., Remizov, A., Roll, R., Fornaçon, K. H., Glassmeier, K. H., Haerendel, G., Hejja, I., … Waesch, R. (2007). ROMAP: Rosetta magnetometer and plasma monitor. *Space Sci. Rev.*, *128*(1-4), 221–240. https://doi.org/10.1007/s11214-006-9033-x

Auster, H. U., Glassmeier, K. H., Magnes, W., Aydogar, O., Baumjohann, W., Constantinescu, D., Fischer, D., Fornaçon, K. H., Georgescu, E., … Wiedemann, M. (2008). The THEMIS fluxgate magnetometer. *Space Sci. Rev.*, *141*(1-4), 235–264. https://doi.org/10.1007/s11214-008-9365-9

Du, A. M., Zhang, Y., Li, H. Y., Qiao, D. H., Yi, Z., Zhang, T. L., Meng, L. F., Ge, Y. S., Luo, H., … Dai, J. L. (2020). The Chinese Mars ROVER fluxgate magnetometers. *Space Sci. Rev.*, *216*(8), 135. https://doi.org/10.1007/s11214-020-00766-8

Finlay, C. C., Kloss, C., Olsen, N., Hammer, M. D., Tøffner-Clausen, L., Grayver, A., and Kuvshinov, A. (2020). The CHAOS-7 geomagnetic field model and observed changes in the South Atlantic Anomaly. *Earth Planets Space*, *72*(1), 156. https://doi.org/10.1186/s40623-020-01252-9

Herčík, D., Auster, H. U., Blum, J., Fornaçon, K. H., Fujimoto, M., Gebauer, K., Güttler, C., Hillenmaier, O., Hördt, A., … Glassmeier, K. H. (2017). The MASCOT magnetometer. *Space Sci. Rev.*, *208*(1), 433–449. https://doi.org/10.1007/s11214-016-0236-5

Hogg, R. V. (1979). An introduction to robust estimation. In R. L. Launer, et al. (Eds.), *Robustness in Statistics* (pp. 1-17). San Diego: Academic Press. https://doi.org/10.1016/B978-0-12-438150-6.50007-8

Jiang, Y., Finlay, C. C., Olsen, N., Tøffner-Clausen, L., Yan, Q., and Zhang, K. (2024). Macau Scientific Satellite-1 initial magnetic field model. *Geophys. Res. Lett.*, *51*(22), e2024GL112305. https://doi.org/10.1029/2024GL112305

Lancaster, E. R., Jennings, T., Morrissey, M., and Langel, R. A. (1980). Magsat vector magnetometer calibration using Magsat geomagnetic field measurements. Goddard Space Flight Center Greenbelt, Maryland 20771: National Aeronautics and Sloace Administration.

Langel, R. A., and Estes, R. H. (1985). Large-scale, near-field magnetic fields from external sources and the corresponding induced internal field. *J. Geophys. Res.*, *90*(B3), 2487–2494. https://doi.org/10.1029/JB090iB03p02487

Merayo, J. M. G., Brauer, P., Primdahl, F., Petersen, J. R., and Nielsen, O. V. (2000). Scalar calibration of vector magnetometers. *Meas. Sci. Technol.*, *11*(2), 120–132. https://doi.org/10.1088/0957-0233/11/2/304

Nielsen, O. V., Petersen, J. R., Primdahl, F., Brauer, P., Hernando, B., Fernandez, A., Merayo, J. M. G., and Ripka, P. (1995). Development, construction and analysis of the 'Ørsted' fluxgate magnetometer. *Meas. Sci. Technol.*, *6*(8), 1099–1115. https://doi.org/10.1088/0957-0233/6/8/004

Olsen, N., Risbo, T., Brauer, P., Merayo, J. M. G., Primdahl, F., and Sabaka, T. (2000a). In-flight calibration methods used for the Ørsted mission. ESA-SP on Calibration of Magnetometers.

Olsen, N., Holme, R., Hulot, G., Sabaka, T., Neubert, T., Tøffner-Clausen, L., Primdahl, F., Jørgensen, J., Léger, J. M., … Voorhies, C. (2000b). Ørsted initial field model. *Geophys. Res. Lett.*, *27*(22), 3607–3610. https://doi.org/10.1029/2000GL011930

Olsen, N. (2002). A model of the geomagnetic field and its secular variation for epoch 2000 estimated from Ørsted data. *Geophys. J. Int.*, *149*(2), 454–462. https://doi.org/10.1046/j.1365-246X.2002.01657.x

Olsen, N., Tøffner-Clausen, L., Sabaka, T. J., Brauer, P., Merayo, J. M. G., Jørgensen, J. L., Léger, J. M., Nielsen, O. V., Primdahl, F., and Risbo, T. (2003). Calibration of the Ørsted vector magnetometer. *Earth Planets Space*, *55*(1), 11–18. https://doi.org/10.1186/BF03352458

Risbo, T., and Olsen, N. (1996). Attitude intercalibration of the star imager and the spherical compact sensor magnetometer for the Ørsted geomagnetic satellite mission. In *Proceedings Volume 2810, Space Sciencecraft Control and Tracking in the New Millennium* (pp. 230–238). Denver, CO, United States: SPIE. https://doi.org/10.1117/12.255145

Risbo, T., Brauer, P., Merayo, J. M. G., Primdahl, F., Balogh, A., and Primdahl, F. (Ed.) (2001). Ørsted Calibration Mission: The Thin Shell Method and Spherical Harmonics Analysis. In *Ground and In-Flight Space Magnetometer Calibration Techniques, ESA SP-490* http://www.oersted.dtu.dk/publications/p.php?233

Yan, Q., Ou, J. M., Suo, L., Jiang, Y., and Liu, P. F. (2023). Study on the estimation of Euler angles for Macau Science Satellite-1. *Earth Planet. Phys.*, *7*(1), 144–150. https://doi.org/10.26464/epp2023017

Zhang, K. (2023). A novel geomagnetic satellite constellation: Science and applications. *Earth Planet. Phys.*, *7*(1), 4–21. https://doi.org/10.26464/epp2023019

Zhang, T. L., Baumjohann, W., Delva, M., Auster, H. U., Balogh, A., Russell, C. T., Barabash, S., Balikhin, M., Berghofer, G., … Lebreton, J. P. (2006). Magnetic field investigation of the Venus plasma environment: Expected new results from Venus Express. *Planet. Space Sci.*, *54*(13-14), 1336–1343. https://doi.org/10.1016/j.pss.2006.04.018